RSC Advances

ROYAL SOCIETY OF CHEMISTRY

www.rsc.org/advances

RSC Advances

ARTICLE

Facile synthesis of $Mn_{6.87}(OH)_3(VO_4)_{3.6}(V_2O_7)_{0.2}$ microtubes and their application as anode materials for lithium-ion batteries

Received 00th January 20xx,
Accepted 00th January 20xx

DOI: 10.1039/x0xx00000x

www.rsc.org/

Shaoyan Zhang* and Yuanyuan Zhang

$Mn_{6.87}(OH)_3(VO_4)_{3.6}(V_2O_7)_{0.2}$ microtubes were successfully synthesized by a simple and facile hydrothermal method without using any surfactants or additives. The reaction conditions influencing the structures and morphologies of the products such as reaction times, reaction temperatures, and pH values were systematically investigated. An Ostwald ripening–dissolution-recrystallization process was proposed to elucidate the formation of the tube-like microstructure. Electrochemical measurements revealed that the as-prepared $Mn_{6.87}(OH)_3(VO_4)_{3.6}(V_2O_7)_{0.2}$ microtubes exhibited high specific capacity, high Coulombic efficiency, and good cycle stability, indicating a promising anode candidate for the application in lithium-ion batteries. Significantly, this is the first report on the $Mn_{6.87}(OH)_3(VO_4)_{3.6}(V_2O_7)_{0.2}$ as anode materials in lithium-ion batteries, and the present work will greatly expand the range of anode choices in lithium-ion batteries.

1. Introduction

Over the past several years, rational synthesis of tubular one-dimensional (1D) nano/microstructures have triggered a worldwide interest because of their unique chemical and physical properties, leading to a wide range of potential applications in nanodevices.[1–5] At the same time, the tubular 1D nano/microstructures have also drawn significant research interest in lithium-ion batteries (LIBs), due to their unique hollow structures and excellent kinetics.[6–10] It has been documented that the large specific surface areas of the unique interior hollow structures and channel-like nano/microstructures can provide large interfacial contact area and short Li^+ transport distance, resulting in superior rate capabilities. Moreover, the central void space of nano/microtubes can not only provide sufficient space to buffer the volume change but also facilitate fast lithium ion diffusion during lithiation/delithiation.[11,12] Inspired by the superiority of the tubular 1D nano/microstructures, much work has been carried out on the synthesis and electrochemical studies of various tubular nano/microstructured materials.[13–16]

As important functional inorganic materials, transition metal vanadates have long been studied as potential battery materials for primary or secondary lithium-ion battery applications owing to their layered nature and excellent kinetics.[17–20] Among them, manganese vanadates (MVOs, also called manganese vanadium oxides) have drawn significant attention owing to their high theoretical capacity, safety and easy preparation. Stimulated by the high electrochemical performance of manganese vanadates, much work has been carried out on the synthesis and electrochemical studies of various manganese vanadates nano/microstructures.[21–24] For example, Huang et al. reported the synthesis of MnV_2O_6 nanobelts through a hydrothermal process at 180 °C for 8 days using $MnCl_2{\cdot}4H_2O$ and commercial V_2O_5 powder as raw materials, which displayed a large reversible capacity of about 630 mA h g^{-1} at a current density of 0.5 A g^{-1}.[25] Inagaki et al. obtained MnV_2O_6 nanorods through a hydrothermal reaction between $Mn(CH_3COO)_2$ and V_2O_5, which exhibited a reversible capacity of about 600 mA h g^{-1} at the current densities of 50 mA g^{-1}.[26] During discharge Mn^{2+} is reduced to Mn^0, and in addition, more than one lithium ion per vanadium can be reacted, giving a high theoretical discharge capacity, greatly expand the range of electrode materials choices.

$Mn_{6.87}(OH)_3(VO_4)_{3.6}(V_2O_7)_{0.2}$ is a complex manganese vanadate phase, which consists of a 3D network with hexagonal and trigonal tunnels.[27] Such a tunnel structure will facilitate the insertion and extraction of Li^+, making $Mn_{6.87}(OH)_3(VO_4)_{3.6}(V_2O_7)_{0.2}$ have potential applications as active materials in LIBs. To the best of our knowledge, up to now, few attempts have been made so far to prepare $Mn_{6.87}(OH)_3(VO_4)_{3.6}(V_2O_7)_{0.2}$ nano/microstructures and study their electrochemical properties. Therefore, developing a facile, economic, and effective strategy to synthesize $Mn_{6.87}(OH)_3(VO_4)_{3.6}(V_2O_7)_{0.2}$ tubular 1D nano/microstructures and then exploring its electrochemical performance toward lithium are of great importance.

In this paper, $Mn_{6.87}(OH)_3(VO_4)_{3.6}(V_2O_7)_{0.2}$ microtubes have been successfully prepared on a large scale via a simple one-step hydrothermal route. The final morphologies of the products were dependent on the reaction conditions, such as the pH values, reaction times, and reaction temperatures. This simple synthetic route, which involved no templates or surfactants, can offer great

College of Chemical Engineering, Shijiazhuang University, Shijiazhuang, 050035, P. R. China. Tel: +86-311-66617326; E-mail: zsyedu@hotmail.com

† Electronic Supplementary Information (ESI) available: XRD pattern and FESEM image of the product obtained at 240 °C, XRD pattern and FESEM images of the product obtained by using $MnCl_2$ as manganese salt, N_2 adsorption/desorption isotherms of the as-prepared $Mn_{6.87}(OH)_3(VO_4)_{3.6}(V_2O_7)_{0.2}$ microtubes and microrods, Cycling performance of the $Mn_{6.87}(OH)_3(VO_4)_{3.6}(V_2O_7)_{0.2}$ microtubes and microrods at a current density of 200 mA g^{-1}. See DOI: 10.1039/x0xx00000x

opportunities for the scale-up preparation of $Mn_{6.87}(OH)_3(VO_4)_{3.6}(V_2O_7)_{0.2}$ nano/microstructures. Moreover, the electrochemical properties of this material as anode materials have been investigated in LIBs. The results showed that the $Mn_{6.87}(OH)_3(VO_4)_{3.6}(V_2O_7)_{0.2}$ microtubes exhibited high specific capacity and good cycling reversibility, indicating promising anode candidates for LIBs.

2. Experimental

2.1 Material Synthesis

All chemicals were of analytical grade and used without further purification. In a typical synthesis, $MnSO_4{\cdot}H_2O$ (0.1692 g) was dissolved into 8 mL of deionized water at room temperature, and 0.3672 g of Na_3VO_4 was dissolved into another 6 mL of deionized water. Then, the Na_3VO_4 solution was added slowly to the $MnSO_4{\cdot}H_2O$ solution under strong magnetic stirring. A brown precipitate formed immediately and the pH value was 10.25. Then, HNO_3 solution (0.5 mL, 1M) was added with magnetic stirring for 10 min to form a precursor suspension with pH of 8.02. The mixture was sealed in a Teflon-lined autoclave (20 mL), heated to 200 °C and maintained at that temperature for 16 h. After the reaction, the autoclave was cooled to ambient temperature naturally. The final products were collected by centrifugation, washed with deionized water and ethanol, and then dried at 80 °C for 12 h. Contrast experiments were carried out by adjusting the pH values of precursors to 6 and 5 by controlling the amount of HNO_3 solution.

2.2 Characterization

The crystalline structures of the products were analyzed with an X-ray diffractometer (XRD, Riguka, Smartlab) with $Cu_{K\alpha}$ radiation (λ=1.5418Å) at a scan rate of 10°/min over the range of 10–60°. The morphologies and microstructures of the as-prepared products were characterized by field-emission scanning electron microscopy (FESEM, Hitachi S-4800) and transmission electron microscopy (TEM, JEOL 2100F). The chemical composition and valence states of element were analyzed using an X-ray photoelectron spectroscope (XPS, Thermo Escalab 250Xi). Brunauer-Emmett-Teller (BET) method was used to measure specific surface areas using N_2 adsorption and desorption isotherms (Micromeritics ASAP 2020 porosimetry system).

2.3 Electrochemical Measurements

The electrochemical performances of the as-prepared $Mn_{6.87}(OH)_3(VO_4)_{3.6}(V_2O_7)_{0.2}$ products were measured using CR2032 coin-type cells at room temperature. The working electrode was fabricated by compressing a mixture of the active material, carbon black, and polyvinylidenefluoride (PVDF) in a weight ratio of active material:carbon black:PVDF=7:2:1. Lithium metal was used as both the counter and reference electrode, and the polypropylene membrane (Celgard 2400) was served as separator. The electrolyte was 1M $LiPF_6$ in a mixture of ethylene carbonate (EC) and dimethyl carbonate (DMC) (v/v=1:1). The galvanostatic discharge–charge tests were carried out on a LAND-CT2001A instrument (Land, China) at 25 mA g^{-1} with a cutoff voltage window of 0.01–3.3V. The impedance measurements were carried out under the open-circuit condition in the frequency range from 1×10^6 to 0.1 Hz using a Gamry Reference 600 potentiostat at room temperature.

3. Results and discussion

The phase and structure of the products were examined by X-ray diffractometer (XRD). Fig. 1 showed the XRD pattern of the $Mn_{6.87}(OH)_3(VO_4)_{3.6}(V_2O_7)_{0.2}$ microtubes obtained under pH of 8 and 200 °C for 16 h. All of the reflections could be readily indexed to pure phase of $Mn_{6.87}(OH)_3(VO_4)_{3.6}(V_2O_7)_{0.2}$ with the hexagonal structure [JCPDS Card No. 50-1796]. The major reflections at 2θ = 13.32°, 23.20°, 26.59°, 26.92°, 31.29°, and 35.66° corresponding to the (110), (030), (121), (220), (040), and (041) planes, respectively, could be seen clearly. No other impurities were detected, indicating the high purity of the product and completed reaction during the process.

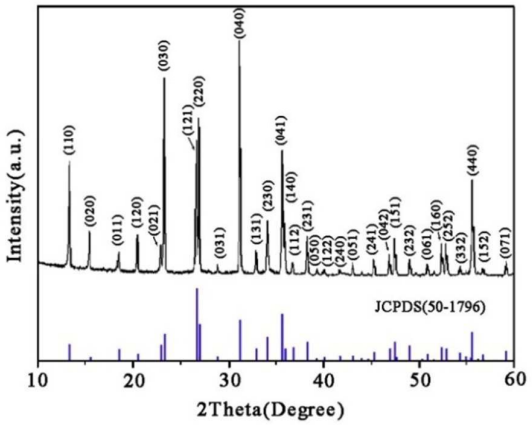

Fig. 1 XRD pattern of the as-prepared $Mn_{6.87}(OH)_3(VO_4)_{3.6}(V_2O_7)_{0.2}$ microtubes.

The morphologies of the as-prepared samples were investigated by field-emission scanning electron microscopy (FESEM). Fig. 2a showed the typical FESEM images of the $Mn_{6.87}(OH)_3(VO_4)_{3.6}(V_2O_7)_{0.2}$ microtubes at relatively low magnification. It indicated that the sample was present in straight tubular structure. The average outer diameter of the open-ended microtubes was approximately 3-5 μm, the length of the nanotubes was tens of micrometers. A higher magnification image (Fig. 2b) showed that the microtubes were open-ended with a rough surface, a lot of tiny nanoparticles were attached on the backbone of the $Mn_{6.87}(OH)_3(VO_4)_{3.6}(V_2O_7)_{0.2}$ microtubes. The wall thickness of the microtubes was about 500-800 nm.

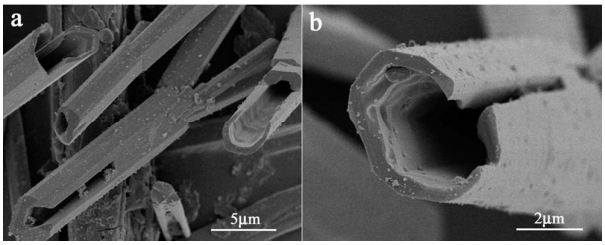

Fig. 2 FESEM images of the as-prepared $Mn_{6.87}(OH)_3(VO_4)_{3.6}(V_2O_7)_{0.2}$ microtubes at different magnifications.

XPS measurement provided further information for the composition and purity of the sample. As shown in Fig. 3a, the survey spectrum demonstrated the presence of Mn, V, and O elements in the $Mn_{6.87}(OH)_3(VO_4)_{3.6}(V_2O_7)_{0.2}$ microtubes. The two strong peaks at 516.4 and 523.9 eV were respectively assigned to V^{5+} 2p3/2 and 2p1/2 (Fig. 3b). The spin-orbit splitting between these two peaks was 7.5 eV, which agreed well with the standard values.[28] Another peak located at 530.1 eV was attributed to O1s. As shown in Fig. 3c, the photoelectron spectrum of O1s could be fitted as two peaks centered at 529.9 and 531.6 eV. The low binding energy component could be attributed to O^{2-} oxidation state bound with Mn or V, while the high binding energy component was associated with the O1s in the hydroxide species.[29,30] It can be seen from Fig. 3d, the high-resolution photoelectron spectra of Mn 2p could be fitted as three peaks centered at 640.7, 646.7 and 652.8 eV. The peaks with the bing energy of 640.7 and 652.8 eV were typical Mn 2p3/2 and Mn 2p1/2 peaks, respectively. As far as the bing energy of Mn^{2+} and Mn^{3+} were contiguous and difficult to be discerned. The concomitant peak located at 646.7 eV was the shakeup satellite peak, which was characteristic of Mn^{2+}. The Mn 3S splitting was widely used for calculating the manganese oxidation state by its satellite separation (ΔE_s).[31] For Mn^{3+} and Mn^{2+} in manganese oxides, ΔE_s (Mn 3s) is 5.3-5.4 and 5.8-6.0 eV, respectively.[31-33] The inset in Fig. 3d showed the ΔE_s (Mn 3s) was 5.7, this value was between the typical ΔE_s for Mn^{3+} and Mn^{2+}, which indicated the coexistence of Mn^{3+} and Mn^{2+} in $Mn_{6.87}(OH)_3(VO_4)_{3.6}(V_2O_7)_{0.2}$. This result was in good agreement with the previous theoretical studies and structural characterization of $(Mn^{2+})_6(Mn^{3+})_{0.87}(OH)_3(VO_4)_{3.6}(V_2O_7)_{0.2}$ by Whittingham.[27]

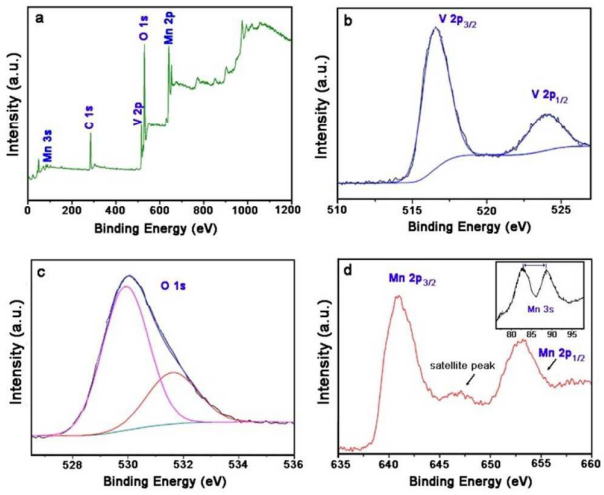

Fig. 3 (a) XPS spectra of $Mn_{6.87}(OH)_3(VO_4)_{3.6}(V_2O_7)_{0.2}$; and (b–d) XPS deconvoluted scans of V 2p, O 1s and Mn 2p, and the inset shows the ΔE_s for Mn 3s.

It was found that the pH values in the reaction system can influence the structure and morphology of the products. Fig. 4 showed the XRD patterns and corresponding morphologies of the products obtained at different pH values. When the pH value of the precursor solution was adjusted to 6 with HNO_3, a new crystal phase, which could be ascribed to $Mn_2V_2O_7$ [JCPDS Card No. 73-1806], began to coexist with $Mn_{6.87}(OH)_3(VO_4)_{3.6}(V_2O_7)_{0.2}$. When adjusting the pH to 5, all of the reflections could be indexed to the pure phase of $Mn_2V_2O_7$. The FESEM images (Fig. 4b and 4c) showed the $Mn_2V_2O_7$ was composed of regular microbricks with typical sizes of about 20–30 μm.

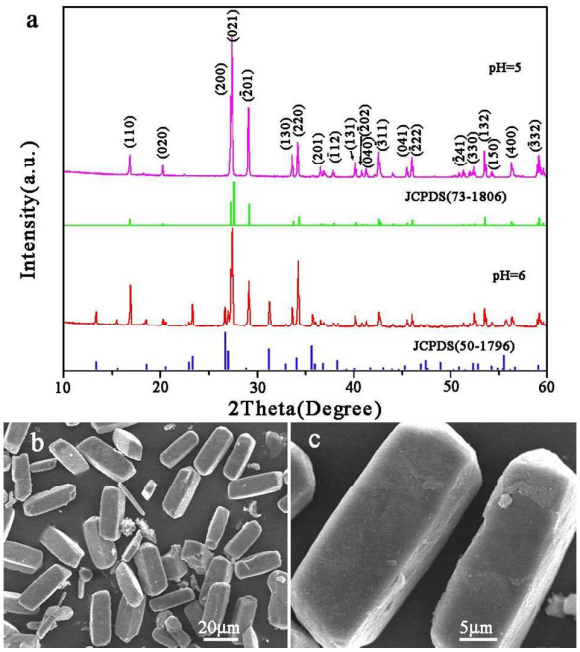

Fig. 4 (a) XRD patterns of the products obtained at pH of 5 and 6; (b,c) FESEM images of the products obtained at pH of 5.

To reveal the growth process of $Mn_{6.87}(OH)_3(VO_4)_{3.6}(V_2O_7)_{0.2}$ microtubes, time-dependent experiments were carried out. Fig. 5 and Fig. 6 showed the XRD patterns and FESEM images of the products obtained at 200 °C for different reaction times. Initially, the direct mixing of $MnSO_4$ and Na_3VO_4 solution at pH=8 led to the formation of a lot of amorphous fine particles (Fig. 5). FESEM image (Fig. 6a,b) showed the diameters of the nanoparticles were about 40 nm. After hydrothermal treatment at 200 °C for 1 h, all the diffraction peaks of the sample could be indexed to a crystalline phase of $Mn_{6.87}(OH)_3(VO_4)_{3.6}(V_2O_7)_{0.2}$. The relatively broader diffraction peaks suggested the smaller crystallite size for $Mn_{6.87}(OH)_3(VO_4)_{3.6}(V_2O_7)_{0.2}$ formed at the early stage. The morphology of the product was shown to be a coexistence of rod-like structures and lots of nanoparticles (Fig. 6c). After a reaction time of 3 h, numerous microrods were observed (Fig. 6d), and the number of particles gradually decreased, suggesting that the longer rods grow at the expense of smaller particles. When the reaction time was prolonged to 6 h, a few small craterlets appeared on the top of some microrods (Fig. 6e,f). Meanwhile, the diffraction peaks were considerably narrowed, suggesting an increase in the crystallite size with further increased reaction time. As the time increased, the craterlets became deeper and bigger, and finally $Mn_{6.87}(OH)_3(VO_4)_{3.6}(V_2O_7)_{0.2}$ microtubes with good crystallinity were obtained after 16 h of hydrothermal reaction (Fig. 2).

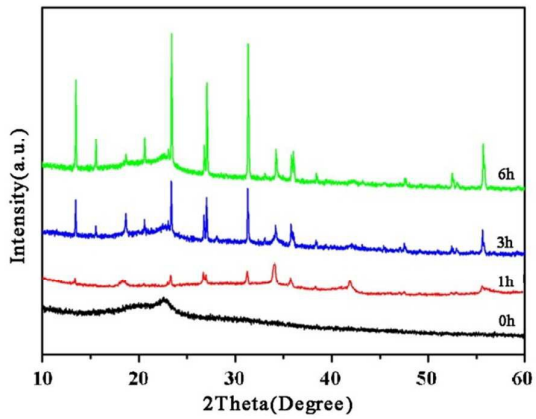

Fig. 5 XRD patterns of the products obtained at different hydrothermal reaction times (0 h, 1 h, 3h, 6h).

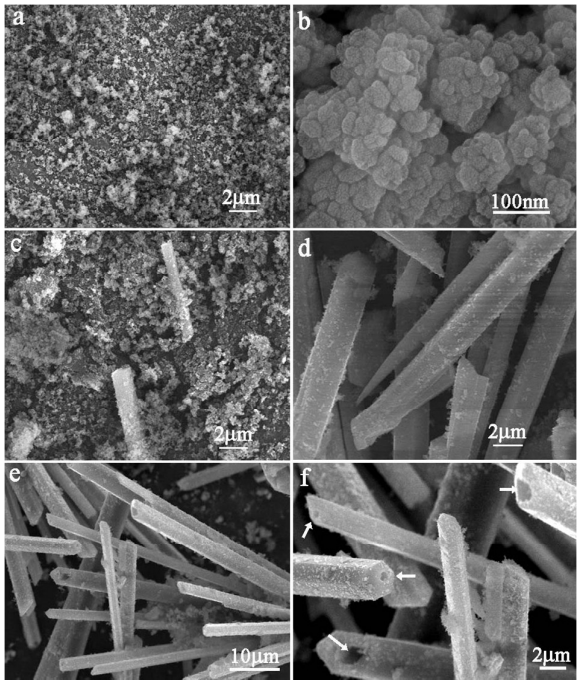

Fig. 6 FESEM images of the products obtained at different hydrothermal reaction times: (a,b) 0h, (c), 1h (d) 3h and (e,f) 6h.

In general, the reaction temperature is another important parameter that can greatly affect the final phase and morphology and microstructure of the product in hydrothermal processes. To investigate the effect of the reaction temperature on the formation of $Mn_{6.87}(OH)_3(VO_4)_{3.6}(V_2O_7)_{0.2}$ microtubes, experiments were carried out under different hydrothermal temperatures while keeping other conditions constant. Fig. 7 showed the XRD patterns and FESEM images of the products obtained at 160 °C and 180 °C. The XRD patterns of the products obtained at different temperature could be identified as the pure and hexagonal structure of $Mn_{6.87}(OH)_3(VO_4)_{3.6}(V_2O_7)_{0.2}$ (Fig. 7a). The morphology of the product obtained at 160 °C was shown to be a coexistence of short nanorods and lots of nanoparticles (Fig. 7b). With an increase in the reaction temperature, the proportion of the 1D structures in the product increased. When the reaction temperature was increased to 180 °C, numerous mesorods were observed and the number of particles decreased (Fig. 7c). The higher magnification image in Fig. 7d showed that the diameter of the rods was in the range of 800–1000 nm and the length was about tens of micrometers. Interestingly, it was noticed that some mesorods attached with each other to form a straw-bundle-like architecture. Fig. 7e displayed a representative TEM image of the as-prepared $Mn_{6.87}(OH)_3(VO_4)_{3.6}(V_2O_7)_{0.2}$ mesorods with the average diameter of about 900 nm and length of tens of micrometers. The high resolution TEM (HRTEM) image of the as-prepared $Mn_{6.87}(OH)_3(VO_4)_{3.6}(V_2O_7)_{0.2}$ mesorods in Fig. 7f showed a distinct lattice fringes with an interplanar spacing of 0.336 nm, matching well with the (121) planes of $Mn_{6.87}(OH)_3(VO_4)_{3.6}(V_2O_7)_{0.2}$. The selected-area electron diffraction (SAED) pattern revealed a spot pattern proving the single-crystal nature of the product. When the temperature was increased to 200 °C, tube-like $Mn_{6.87}(OH)_3(VO_4)_{3.6}(V_2O_7)_{0.2}$ microstructures were obtained (Fig. 2). After hydrothermal reaction at 240 °C for 6h, $Mn_{6.87}(OH)_3(VO_4)_{3.6}(V_2O_7)_{0.2}$ microtubes were also obtained (see the Supporting Information, Fig. S1 and S2). These results suggested that the relative higher reaction temperature was favorable for the formation of $Mn_{6.87}(OH)_3(VO_4)_{3.6}(V_2O_7)_{0.2}$ microtubes. Parallel experiments were carried out by substituting $MnSO_4$ with $MnCl_2$. $Mn_{6.87}(OH)_3(VO_4)_{3.6}(V_2O_7)_{0.2}$ tubular microstructures were also observed under similar hydrothermal conditions, as shown in Fig. S3 and S4. It is widely accepted that the specific surface area and pore volume of the nano/microstructured materials depend intimately on their morphologies and sizes. To reveal the correlation between the specific surface area and morphology of the sample, the Brunauer–Emmett–Teller (BET) surface area, N_2-adsorption/desorption isotherms, and the pore volume study for the $Mn_{6.87}(OH)_3(VO_4)_{3.6}(V_2O_7)_{0.2}$ microtubes and microrods (obtained at 200 °C for 3h) were given in Fig. S5 and Table S1. The BET surface area of the $Mn_{6.87}(OH)_3(VO_4)_{3.6}(V_2O_7)_{0.2}$ microtubes was calculated to be 19.4 $m^2 g^{-1}$, which is much higher than that of the microrods (5.4 $m^2 g^{-1}$). The total pore volume of the microtubes and microrods was 0.1159 and 0.0177 $cm^3 g^{-1}$, respectively. Evidently, the $Mn_{6.87}(OH)_3(VO_4)_{3.6}(V_2O_7)_{0.2}$ microtubes exhibited larger pore volume and much higher specific surface than the microrods, which is beneficial to electrochemical applications.

In the present synthesis, neither surfactants nor templates were introduced in the reaction system. On the basis of the above experimental results, the formation mechanism for the $Mn_{6.87}(OH)_3(VO_4)_{3.6}(V_2O_7)_{0.2}$ microtubes can be simply depicted as an Ostwald ripening–dissolution-recrystallization process (Fig. 8). In the initial stage, $Mn_{6.87}(OH)_3(VO_4)_{3.6}(V_2O_7)_{0.2}$ nuclei were produced, aggregated, and grown into rod-like nano/microstructures, as indicated by the sample at early stages (Fig. 6a-d). This process is in accordance with the well-known "Ostwald ripening mechanism".[34,35] With the reaction processing, "a dissolution-recrystallization process" occurs. Because of the different rate between the dissolution and recrystallization process under the hydrothermal conditions, simultaneous formation of many hexagonal phase $Mn_{6.87}(OH)_3(VO_4)_{3.6}(V_2O_7)_{0.2}$ seeds will greatly reduce the concentration of $Mn_{6.87}(OH)_3(VO_4)_{3.6}(V_2O_7)_{0.2}$ in the bulk

solution. Therefore, it could not provide enough $Mn_{6.87}(OH)_3(VO_4)_{3.6}(V_2O_7)_{0.2}$ molecules for the growth of the growing $Mn_{6.87}(OH)_3(VO_4)_{3.6}(V_2O_7)_{0.2}$ microrod. Mass transportation to the growing regions would lead to undersaturation in the central part of the growing faces of each seeds; thus, small craterlets appeared on the top of some $Mn_{6.87}(OH)_3(VO_4)_{3.6}(V_2O_7)_{0.2}$ microrods. As the reaction proceeded further, $Mn_{6.87}(OH)_3(VO_4)_{3.6}(V_2O_7)_{0.2}$ microtubes with a well-defined hollow interior structure were obtained due to the dissolution process preferentially occurring in the center of rod-like crystal and deepening gradually into the depth of the crystal. A similar mechanism was reported by Xia and co-workers in the case of fabricating tellurium nanotubes with well-controlled structures.[36] The phenomenon was also observed in $BiVO_4$ microtubes,[37] ZnO crystalline microtubes[38] and Cu(TCNQ) (TCNQ=7,7,8,8-tertracyno-p-quinodimethane) microtubes[39].

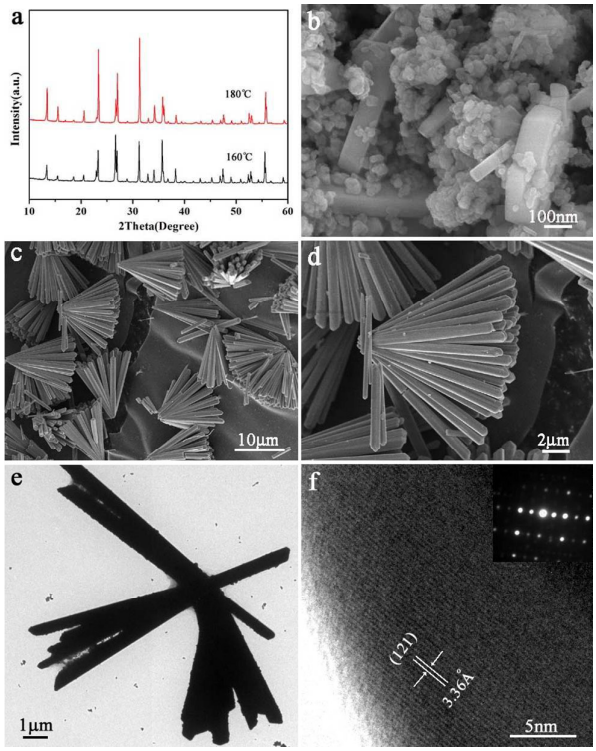

Fig. 7 (a) XRD patterns, (b)–(d) FESEM and (e, f) TEM images of the products obtained at different temperatures: (b) 160 °C and (c-f) 180 °C. The inset in (f) is the SAED pattern.

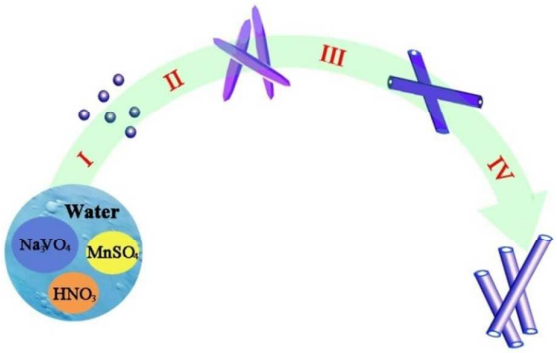

Fig. 8 Schematic illustration of the formation process of the $Mn_{6.87}(OH)_3(VO_4)_{3.6}(V_2O_7)_{0.2}$ microtubes. (I) Formation of crystal nucleus of $Mn_{6.87}(OH)_3(VO_4)_{3.6}(V_2O_7)_{0.2}$ at initial stage under hydrothermal reaction condition; (II) Formation of $Mn_{6.87}(OH)_3(VO_4)_{3.6}(V_2O_7)_{0.2}$ microrods; (III) Craterlet generation at the top of $Mn_{6.87}(OH)_3(VO_4)_{3.6}(V_2O_7)_{0.2}$ microrods; (IV) Formation of $Mn_{6.87}(OH)_3(VO_4)_{3.6}(V_2O_7)_{0.2}$ microtubes.

To investigate the application of the as-prepared $Mn_{6.87}(OH)_3(VO_4)_{3.6}(V_2O_7)_{0.2}$ microtubes in LIBs, the products were configured as electrodes to evaluate their electrochemical properties. For comparison purposes, we also evaluated the electrochemical performance of the $Mn_{6.87}(OH)_3(VO_4)_{3.6}(V_2O_7)_{0.2}$ microrods obtained at 200 °C for 3h (Fig. 6d). Fig. 9a depicted the comparative cycling performances of $Mn_{6.87}(OH)_3(VO_4)_{3.6}(V_2O_7)_{0.2}$ microtubes and microrods and the Coulombic efficiency of $Mn_{6.87}(OH)_3(VO_4)_{3.6}(V_2O_7)_{0.2}$ microtubes with a voltage window of 0.01–3.3 V at a current density of 25 mA g^{-1}. Clearly, a reversible capacity of 643 mA h g^{-1} can be delivered by microtubes up to 50 cycles, which was about 1.2 times of that for microrods (519 mA h g^{-1}). Additionally, the rate capability of the $Mn_{6.87}(OH)_3(VO_4)_{3.6}(V_2O_7)_{0.2}$ microtubes was also much better than that of microrods, as shown in Fig. 9b. At a high current density of 200 mA g^{-1}, the $Mn_{6.87}(OH)_3(VO_4)_{3.6}(V_2O_7)_{0.2}$ microtubes manifested a capacity of 392 mA h g^{-1}, whereas a capacity of only 251 mA h g^{-1} was delivered by microrods. When the current density was reduced back to be 50 mA g^{-1}, $Mn_{6.87}(OH)_3(VO_4)_{3.6}(V_2O_7)_{0.2}$ microtubes still can deliver a reversible capacity of 551 mA h g^{-1}, implying a stable electrode structure even under the high current density. To further compare the cycling performance of $Mn_{6.87}(OH)_3(VO_4)_{3.6}(V_2O_7)_{0.2}$ microtubes and microrods at high current density, the discharge capacity with cycling at a current density of 200 mA g^{-1} were tested (Fig. S6). After 100 cycles, the microtube electrode retained 363 mA h g^{-1}, while the microrod electrode showed a relatively lower reversible capacity of 216 mA h g^{-1}. Fig. 9c displayed the discharge–charge curves of the $Mn_{6.87}(OH)_3(VO_4)_{3.6}(V_2O_7)_{0.2}$ microtubes in the initial three cycles in the voltage range of 0.01–3.3 V at a current density of 25 mA g^{-1}. The initial discharge–charge capacity of the $Mn_{6.87}(OH)_3(VO_4)_{3.6}(V_2O_7)_{0.2}$ microtubes was 1159/802 mA h g^{-1}, leading to a large initial irreversible loss of about 30.8 %. In the second cycle, the discharge and charge capacities were found to be 775 and 733 mA h g^{-1}, respectively, corresponding to a higher Coulombic efficiency of 94.6 % (Fig. 9a). Moreover, the Coulombic efficiency of microtubes quickly increased in the subsequent cycles and retained about 98.6 % after 50 cycles. Thus, it is obvious that the as-prepared $Mn_{6.87}(OH)_3(VO_4)_{3.6}(V_2O_7)_{0.2}$ microtube electrode shows better cycling stability and lithium storage properties. Based on the discharge–charge results and the previous studies of the related manganese vanadate systems, we propose that the discharge-charge mechanism is similar to MnV_2O_6.[26,40] During the discharging process, the Mn^{2+} and Mn^{3+} is reduced to Mn^0, and V^{5+} is reduced to V^{4+} and further to V^{3+}. On the contrary, the metallic Mn is oxidized to Mn^{2+} and V^{3+} is oxidized to V^{5+} during the subsequent charging process. However, with the formation of Mn^0 in the initial discharging process, most of Mn releases from the framework, which induces large strains in the MVO host material and leads to volume change and fracture. Due to the structure

transformation, part of Mn^0 cannot return to the host in the subsequent charging process. Therefore, the large irreversible capacity loss in the first cycle may be partially attributed to the formation of a solid electrolyte inter-phase film (SEI) onto the surface of the electrode materials. Furthermore, the irreversible structure transformation associated with the formation/annihilation of manganese particles during the discharge–charge process may also cause irreversible capacity loss.[41,42] Similar results have also been observed in many transition metal vanadats, such as MnV_2O_6,[26] $Cu_{1.1}V_4O_{11}$,[43] CoV_2O_6,[44] $FeVO_4$.[45]

To provide a deeper insight into the effect of morphology on the electrochemical performance of $Mn_{6.87}(OH)_3(VO_4)_{3.6}(V_2O_7)_{0.2}$, electrochemical impedance spectroscopy (EIS) measurements of the $Mn_{6.87}(OH)_3(VO_4)_{3.6}(V_2O_7)_{0.2}$ microtubes and microrods were carried out and shown in Fig. 9d. The spectra of the two electrodes had a similar shape with one depressed semicircle in the high frequency regions and an inclined line in the low-frequency region. The semicircle can be assigned to the combination of Li^+ migration resistance through the SEI film and the charge-transfer resistance at the electrode surface, and the linear portion can be assigned to the solid-state diffusion resistance of lithium ions within the host.[46–48] Apparently, the semicircle diameter of the $Mn_{6.87}(OH)_3(VO_4)_{3.6}(V_2O_7)_{0.2}$ microtubes was much smaller than that of $Mn_{6.87}(OH)_3(VO_4)_{3.6}(V_2O_7)_{0.2}$ microrods, indicating that $Mn_{6.87}(OH)_3(VO_4)_{3.6}(V_2O_7)_{0.2}$ microtubes had much lower SEI resistance and charge-transfer resistance. Therefore, the unique interior hollow structure was beneficial for enhancing the reaction kinetics, thus leading to higher reversible capacity and better cyclability.

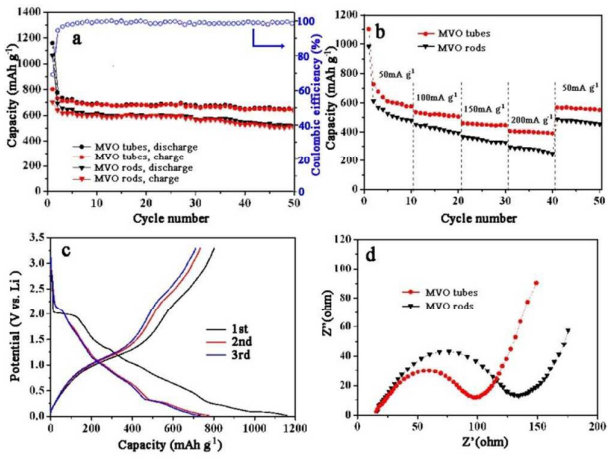

Fig. 9 (a) Cycling performance of the $Mn_{6.87}(OH)_3(VO_4)_{3.6}(V_2O_7)_{0.2}$ microtubes and microrods at a current density of 25 mA g^{-1}, (b) Rate capability of the $Mn_{6.87}(OH)_3(VO_4)_{3.6}(V_2O_7)_{0.2}$ microtubes and microrods at various current density from 50 to 200 mA g^{-1}. (c) Discharge/charge profiles of the $Mn_{6.87}(OH)_3(VO_4)_{3.6}(V_2O_7)_{0.2}$ microtubes, (d) Nyquist plots for $Mn_{6.87}(OH)_3(VO_4)_{3.6}(V_2O_7)_{0.2}$ microtubes and microrods.

According to the results presented above, the as-prepared $Mn_{6.87}(OH)_3(VO_4)_{3.6}(V_2O_7)_{0.2}$ microtubes exhibited superior electrochemical performances in terms of Coulombic efficiency, specific capacity, and cycling performance, which is of great significance for LIBs. We believe the better electrochemical performances of the $Mn_{6.87}(OH)_3(VO_4)_{3.6}(V_2O_7)_{0.2}$ microtubes can be attributed to the unique interior hollow structures and channel-like morphology. Specifically, the central void space of $Mn_{6.87}(OH)_3(VO_4)_{3.6}(V_2O_7)_{0.2}$ microtubes can not only provide sufficient space to buffer the volume change but also facilitate fast lithium ion diffusion during lithiation/delithiation. Meanwhile, the relatively large surface area of $Mn_{6.87}(OH)_3(VO_4)_{3.6}(V_2O_7)_{0.2}$ microtubes provides a large amount of reactive sites and thus enhances the contact between the active material and the electrolyte. In addition, the unique channel-like nanostructures also benefit in retaining the structural stability and partially accommodating the pulverization of electrode.

4. Conclusions

In summary, $Mn_{6.87}(OH)_3(VO_4)_{3.6}(V_2O_7)_{0.2}$ microtubes were successfully prepared by a simple and convenient hydrothermal method. The unique morphology and structural feature of $Mn_{6.87}(OH)_3(VO_4)_{3.6}(V_2O_7)_{0.2}$ were significantly influenced by the reaction times, reaction temperatures, and pH values. According to comparative experimental results, an Ostwald ripening–dissolution-recrystallization process was proposed to elucidate the formation of the tube-like microstructure. Electrochemical evaluation revealed that the $Mn_{6.87}(OH)_3(VO_4)_{3.6}(V_2O_7)_{0.2}$ microtubes exhibited higher discharge capacity and better cyclability than the $Mn_{6.87}(OH)_3(VO_4)_{3.6}(V_2O_7)_{0.2}$ microrods. The reversible capacity of 643 mA h g^{-1} was delivered after 50 cycles at a current density of 25 mA g^{-1}, with Coulombic efficiency of about 98.6 %. The present work will greatly expand the range of anode choices and could assist long-term endeavors in developing high capacity anode materials for LIBs. Furthermore, the $Mn_{6.87}(OH)_3(VO_4)_{3.6}(V_2O_7)_{0.2}$ nanostructure may also find potential applications in other fields, such as catalysis, semiconductor, water purification, and so on.

Acknowledgements

This work was supported by the National Natural Science Foundation of China (No. 21303107), Natural Science Foundation of Hebei Province (No. B2014106056, B2010001946), and Program of "One Hundred Innovative Talents" of Higher Education Institutions of Hebei Province (No. BR2-264).

Notes and references

1 D. Li, Y. L. Wang and Y. N. Xia, *Adv. Mater.*, 2004, **16**, 361.
2 Y. Qin, X. D.Wang and Z. L.Wang, *Nature*, 2008, **451**, 809.
3 S. A. Needham, G. X. Wang and H. K. Liu, *J. Power Sources*, 2006, **159**, 254.
4. Y. F. Tang, Z. Q. Liu, X. J. Lü, B. F. Wang and F. Q. Huang, *RSC Adv.*, 2014,**4**, 36372.
5. P. F. Gao, H. P. Jia, J. Yang, Y. Nuli, J. L. Wang and J. Chen, *Phys. Chem. Chem. Phys.,* 2011, **13**, 20108.
6 L. L. Li, S. J. Peng, J. Wang, Y. L. Cheah, P. Teh, Y. Ko, C. Wong and M. Srinivasan, *ACS Appl. Mater. Interfaces*, 2012, **4**, 6005.

7 X. W. Lou, D. Deng, J. Y. Lee, J. Feng and L. A. Archer, *Adv. Mater.*, 2008, **20**, 258.
8 X. X. Li, F. Y. Cheng, B. Guo and J. Chen, *J. Phys. Chem. B*, 2005, **109**, 14017.
9 J. Chen, L. N. Xu, W. Y. Li and X. L. Gou, *Adv. Mater.*, 2005, **17**, 582.
10 B. J. Landi, M. J. Ganter, C. D. Cress, R. A. Dileo and R. P. Raffaelle, *Energy Environ. Sci.*, 2009, **2**, 638.
11 L. L. Li, S. J. Peng, Y. L. Cheah, J. Wang, P. F. Teh, Y. Ko, C. Wong and M. Srinivasan, *Nanoscale*, 2013, **5**, 134.
12 F. Y. Cheng , Z. L. Tao , J. Liang and J. Chen, *Chem. Mater.*, 2008, **20**, 667.
13 X. B. Huang, X. Li, H. Y. Wang, Z. L. Pan, M. Z. Qu and Z. L. Yu, *Electrochim. Acta*, 2010, **55**, 7362.
14 W. Y. Li, L. N. Xu and J. Chen, *Adv. Funct. Mater.*, 2005, **15**, 851**.**
15 Y. Wang, H. C. Zeng and J. Y. Lee, *Adv. Mater.*, 2006, **18**, 645.
16 Y. B. Fu, R. B. Ma, Y. Shu, Z. Cao and X. H. Ma, *Mater. Lett.*, 2009, **63**, 1946.
17 L. H. Gan, D. R. Deng, Y. J. Zhan, G. Li, X. Y. Wang, L. Jiang and C. R. Wang, *J. Mater. Chem. A*, 2014, **2**, 2461.
18 Y. Tang, J. Zhou, J. Liu, L. X. Liu and S. Q. Liang, *Int. J. Electrochem. Sci.*, 2013, **8**, 1138.
19 F. Y. Cheng and J. Chen, *J. Mater. Chem.*, 2011, **21**, 9841.
20 Y. P. Guo, H. Ohsato and K. I. Kakimoto, *J. Eur. Ceram. Soc.*, 2006, **26**, 1827.
21 S. Y. Zhang, R. S. Hu, L. Liu and D. Y. Wang, *Mater. Lett.*, 2014, **124**, 57.
22 F. Zhang and M. S. Whittingham, *Electrochem. Commun.*, 2000, **2**, 69.
23 Y. Piffard, F. Leroux, D. Guyomard, J. -L. Mansot and M. Tournoux, *J. Power Sources*, 1997, **68**, 698.
24 D. Hara, J. Shirakawa, H. Ikuta, Y. Uchimoto, M. Wakihara, T. Miyanaga and I. Watanabe, *J. Mater. Chem.*, 2002, **12**, 3717.
25 W. D. Huang, S. K. Gao, X. K. Ding, L. L. Jiang and M. D. Wei, *J. Alloy. Compd.*, 2010, **495**, 185.
26 T. Morishita, H. Konno, Y. Izumi and M. Inagaki, *Solid State Ionics*, 2006, **177**, 1347.
27 F. Zhang, P. Y. Zavalij and M. S. Whittingham, *J. Mater. Chem.*, 1999, **9**, 3137.
28 G. E. Muilenbenger, *Handbook of X-ray photoelectron Spectroscopy*, Perkin-Elmer Corporation, Eden Prarie, MN, 1979.
29 C. D. Wagner, D. E. Passoja, H. F. Hillery, T. G. Kinisky, H. A. Six, W. T. Jansen, J. A. Taylor, *J. Vac. Sci. Technol.*, 1982, **21**, 933.
30 S. B. Ni, X. H. Wang, X. L. Sun, F. Yang, Y. Q. Liu, D. Y. He, *Mater. Chem. Phys.*, 2010, **124**, 803.
31 M. Toupin, T. Brousse, D. Belanger, *Chem. Mater.*, 2004, **16**,3184.
32 S. W. Lee, J.Kim, S. Chen, P. T. Hammond, Y. Shao-Horn, *ACS Nano*, 2010, **4**, 3889.
33 V. Subramanian, H. W. Zhu, B. Q. Wei, *Chem. Phys. Lett.*, 2008, **453**, 242.
34 Z. A. Peng and X. G. Peng, *J. Am. Chem. Soc.*, 2001, **123**, 1389.
35 A. Yella, U. K. Gautam, E. Mugnaioli, M. Panthöfer, Y. Bando, D. Golberg, U. Kolb and W. Tremel, *CrystEngComm*, 2011, **13**, 4074.
36 B. Mayers and Y. N. Xia, *Ad*V. *Mater.*, 2002, **14**, 279.
37 L. Zhou, W. Z. Wang, L. S. Zhang, H. L. Xu and W. Zhu, *J. Phys. Chem. C*, 2007, **111**, 13659.
38 L. Vayssieres, K. Keis, A. Hagfeldt and S. E. Lindquist, *Chem. Mater.*, 2001, **13**, 4395.
39 X. H. Zhou, S. J. Wei and S. S. Zhang, *Langmuir*, 2008, **24**, 4464.
40 F. Hu, C. H. Zhang, S. Zhang, X. Ming, G. Chen, Y. J. Wei and C. Z. Wang, Chem. *Res. Chinese Universities*, 2011, **27**, 528.
41 D. Aurbach, B. Markovsky, M. D. Levi, E. Levi, A. Schechter, M. Moshkovich and Y. Cohen, *J. Power Sources*, 1999, **81–82**, 95.
42 A. Rong, X. P. Gao, G. R. Li, T. Y. Yan, H. Y. Zhu, J. Q. Qu and D. Y. Song, *J. Phys. Chem. B*, 2006, **110**, 14754.
43 M. Morcrette, P. Martin, P. Rozier, H. Vezin, F. Chevallier, L. Laffont, P. Poizot and J.-M. Tarascon, *Chem. Mater.*, 2005, **17**, 418.
44 S. Laruelle, P. Poizot, E. Baudrin, V. Briois, M. Touboul and J.-M. Tarascon, *J. Power Sources*, 2001, **97–98**, 251.
45 P. Poizot, E. Baudrin, S. Laruelle, L. Dupont, M. Touboul and J.-M. Tarascon, *Solid State Ion*., 2001, **38**, 31.
46 L. Q. Mai, X. Xu, C. H. Han, Y. Z. Luo, L. Xu, Y. M. Wu and Y. L. Zhao, *Nano Lett.*, 2011, **11**, 4992.
47 S. Y. Zhang, L. Ren and S. J. Peng, *CrystEngComm*, 2014, **16**, 6195.
48 C. L. Zhang, H. S. Li, N. Ping, G. Pang, G. Y. Xu and X. G. Zhang, *RSC Adv.*, 2014, **4**, 38791.